Journal of
Applied Remote Sensing

RemoteSensing.SPIEDigitalLibrary.org

Improving iterative surface energy balance convergence for remote sensing based flux calculation

Ramesh Dhungel
Richard G. Allen
Ricardo Trezza

SPIE.

Ramesh Dhungel, Richard G. Allen, Ricardo Trezza, "Improving iterative surface energy balance convergence for remote sensing based flux calculation," *J. Appl. Remote Sens.* **10**(2), 026033 (2016), doi: 10.1117/1.JRS.10.026033.

Improving iterative surface energy balance convergence for remote sensing based flux calculation

Ramesh Dhungel,[a,*] Richard G. Allen,[b] and Ricardo Trezza[b]
[a]University of California, School of Engineering, Merced, California 95343, United States
[b]University of Idaho, Kimberly Research and Extension Center, Department of Biological and Agricultural Engineering, Kimberly, Idaho 83341, United States

Abstract. A modification of the iterative procedure of the surface energy balance was purposed to expedite the convergence of Monin–Obukhov stability correction utilized by the remote sensing based flux calculation. This was demonstrated using ground-based weather stations as well as the gridded weather data (North American Regional Reanalysis) and remote sensing based (Landsat 5, 7) images. The study was conducted for different land-use classes in southern Idaho and northern California for multiple satellite overpasses. The convergence behavior of a selected Landsat pixel as well as all of the Landsat pixels within the area of interest was analyzed. Modified version needed multiple times less iteration compared to the current iterative technique. At the time of low wind speed (~1.3 m/s), the current iterative technique was not able to find a solution of surface energy balance for all of the Landsat pixels, while the modified version was able to achieve it in a few iterations. The study will facilitate many operational evapotranspiration models to avoid the nonconvergence in low wind speeds, which helps to increase the accuracy of flux calculations. © *2016 Society of Photo-Optical Instrumentation Engineers (SPIE)* [DOI: 10.1117/1.JRS.10.026033]

Keywords: numerical solution; remote sensing based evapotranspiration; Monin–Obukhov similarity; surface energy balance; iterative technique.

Paper 15804L received Nov. 19, 2015; accepted for publication May 10, 2016; published online Jun. 9, 2016.

1 Introduction

The development of remote sensing based surface energy balance algorithms were facilitated to calculate evapotranspiration (ET) in larger spatial and temporal resolutions. The accuracy of these remote sensing based ET calculations is largely dominated by precise atmospheric corrections, emissivity estimations, high accuracy in sensor calibration, and other numerous land surface parameters.[1] Accurate estimation of ET is vital for many hydrological applications, especially in semiarid and arid environments for managing scarce water resources, and to cope with a changing climate.[2–14] Approximately 90% of annual precipitation is represented by ET in semiarid and arid regions.[15,16] While calculating ET, operational ET models such as mapping evapotranspiration at high resolution and internalized calibration (METRIC),[17] surface energy balance algorithm for land (SEBAL),[18] and surface energy balance system (SEBS)[19] depend on an iterative procedure for the convergence of the surface energy balance components and Monin–Obukhov (MO) stability correction. However, low wind speed (<2 m/s) creates a nonconvergence, lack of closure,[20,21] and inaccuracy in the surface energy balance and the MO similarity correction, which has been widely discussed.[22–28] With weak winds, turbulence periodically vanishes allowing the shear to grow locally. This leads to a complicated, nonstationary pattern, where MO flux-gradient relationships fail when applied to individual cases.

In METRIC and SEBAL, the convergence of hot and cold pixels is generally achieved within 10 iterations, but when wind speed is low (<2 m/s at 200 m height), they may need a larger number of iterations or sometimes be in a state of nonconvergence. In the instances of

*Address all correspondence to: Ramesh Dhungel, E-mail: rdhungel@ucmerced.edu

nonconvergence, these models sometimes achieve convergence by increasing the wind speed. An increase in wind speed generally elevates the ET rate by mechanical mixing.[29,30] This nonconvergence not only decreases the efficiency and increases the computational time, but also can decrease the accuracy of surface energy balance components (i.e., underestimation or overestimation of the fluxes) along with ET calculation. In semiarid areas, efficient irrigation practices are largely dominated by accurate ET calculation,[31–36] so it is important to address the problem of nonconvergence.

Ács and Kovács[25] declared that the number of iterations for the convergence of surface energy balance largely depends on the meteorological conditions. They found that the convergence was usually achieved in <10 iterations in both moderately stable and unstable conditions. But when atmospheric conditions are strongly unstable, close to or at the boundary of free convection zone (extremely small wind and large difference in surface-air temperature), the convergence can be >200. They also indicated that in a strong, stable condition with low wind speed, i.e., <1 m/s, it can take 100 iterations or more to converge. Numerous researchers have contributed different methods for developing methods for solving the energy balance and the MO stability correction function with and without iteration procedures.[37–41] The majority of these iterative and noniterative procedures use the Richardson number to estimate a stability parameter ($\xi = z/L$, z is the blending height and L is the MO similarity length). Iteration of the MO length (L) for stability correction can be costly in terms of CPU time in numerical simulations of regional atmospheric models.[42] Global forecasting and climate models use approximate explicit functions rather than the original stability function to increase computational efficiency.[39] These methods need a fitting polynomial for the solution of equations to estimate the Obukhov stability parameter (ξ) using the Richardson number. These kinds of regression techniques develop numerous fitting coefficients according to different meteorological conditions combined with the Richardson number, which may not be feasible for many operational ET models. The current iterative technique can be computationally inefficient, time-consuming, and may frequently face a situation of nonconvergence, especially when dealing with a higher temporal and spatial resolution dataset in a low wind speed. To overcome this problem, Dhungel et al.[43] proposed a backward-averaged iterative technique to expedite the convergence of the remote sensing based surface flux calculation. The major objective of this study is to demonstrate the improved convergence behavior of the surface energy components for various meteorological conditions.

2 Material and Methods

2.1 *Study Area*

The study was conducted for different Landsat satellite overpass dates (May 17, 2008, June 18, 2008, June 27, 2010, and August 22, 2010) in southern Idaho near American Falls (path 39, row 40) and northern California (path 44, row 34). Figure 1(a) shows the study area located in southern Idaho along with a Landsat image of May 17, 2008, and North American Regional Reanalysis (NARR) boundary with an area of interest of ~1048 km^2 (State of Idaho), while Fig. 1(b) shows the California study area. The study area in Fig. 1(a) is the size of a single NARR pixel, which is 32 km × 32 km, corresponding to about a million Landsat pixels. This study area is bordered with three other NARR pixels with different meteorological conditions. A National Land Cover Database (NLCD) is used to determine the land-use classes. The forcing data from NARR (Mesinger et al.[44]) were air temperature (T_a) at a 30 m height, wind speed (u_z) at 30 m, specific humidity (q_a) at 30 m, incoming shortwave ($R_{s\downarrow}$) at the surface, and incoming long-wave radiation ($R_{L\downarrow}$) at the surface. The data acquired from the METRIC model output were estimates for albedo (α), roughness length of momentum transfer (Z_{om}), broadband emissivity (ε_o), surface temperature (T_s), and leaf area index (LAI) at the satellite overpass dates [shown at the top of Fig. 2(b)].

3 Methodology

The aerodynamic equation of sensible heat flux (H) is shown in Eq. (1). Equation (1) can be inverted to calculate dT [Fig. 2(a)] or H, T_s [Fig. 2(b)] or as per the availability of data and the

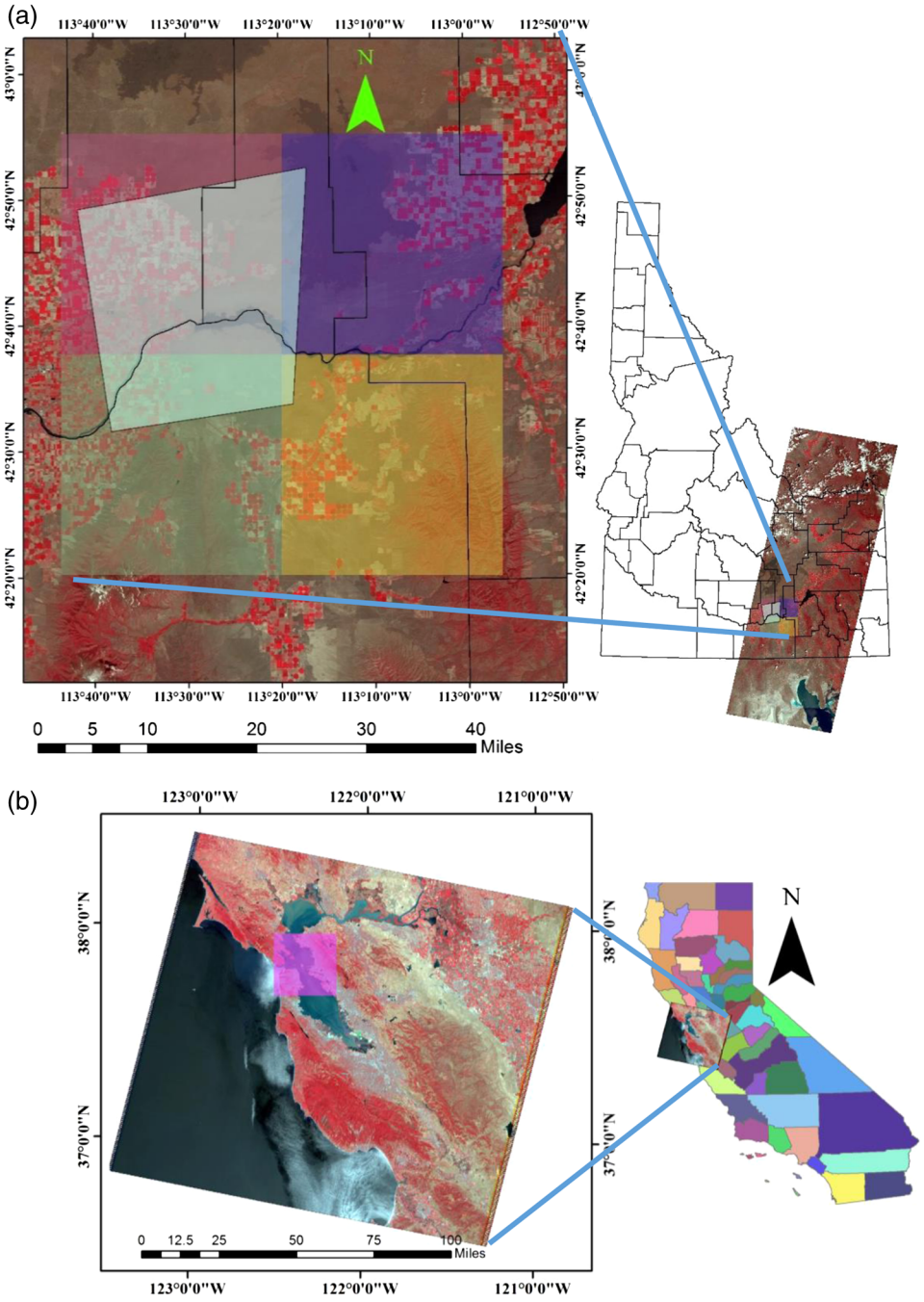

Fig. 1 Study area inside the Landsat image in (a) southern Idaho on May 17, 2008, NARR data and Idaho map (right), and (b) northern California on June 27, 2010.

adopted procedure. Aerodynamic resistance is difficult to quantify and it is computed indirectly with various components. Any error in r_{ah} would directly affect the final value of H and dT.

$$H = \rho_a c_p \frac{\mathrm{d}T}{r_{ah}} = \rho_a c_p \frac{T_s - T_a}{r_{ah}}, \tag{1}$$

where dT is the temperature difference between two different heights, T_s is the surface temperature (K), T_a is the air temperature (K), c_p is the specific heat capacity of air [J/(kg K)], ρ_a is the

density of moist air (kg/m^3), and r_{ah} is the aerodynamic resistance (s/m). Surface temperature (T_s) in the gridded form can be estimated from the thermal band of satellite or iteratively calculated inside the surface energy balance. METRIC, SEBAL, and many other operational models utilize the thermal band of the satellite to estimate T_s. In this technical note, we focused on the numerical convergence of existing stability correction utilized in the surface energy balance. The primary components that help to accelerate the convergence process were determined by the sensitivity analyses, but backward averaging of the components of the surface energy balance that are in the nested loops facilitated the convergence process.

3.1 *Case I—Surface Temperature (T_s) from Thermal Band (Satellite Overpass)*

To demonstrate the improvement, (1) we adopted an identical procedure that is utilized to calculate dT and r_{ah} for hot and cold pixels [Fig. 2(a)] and (2) once dT_{hot} and dT_{cold} are known, dT

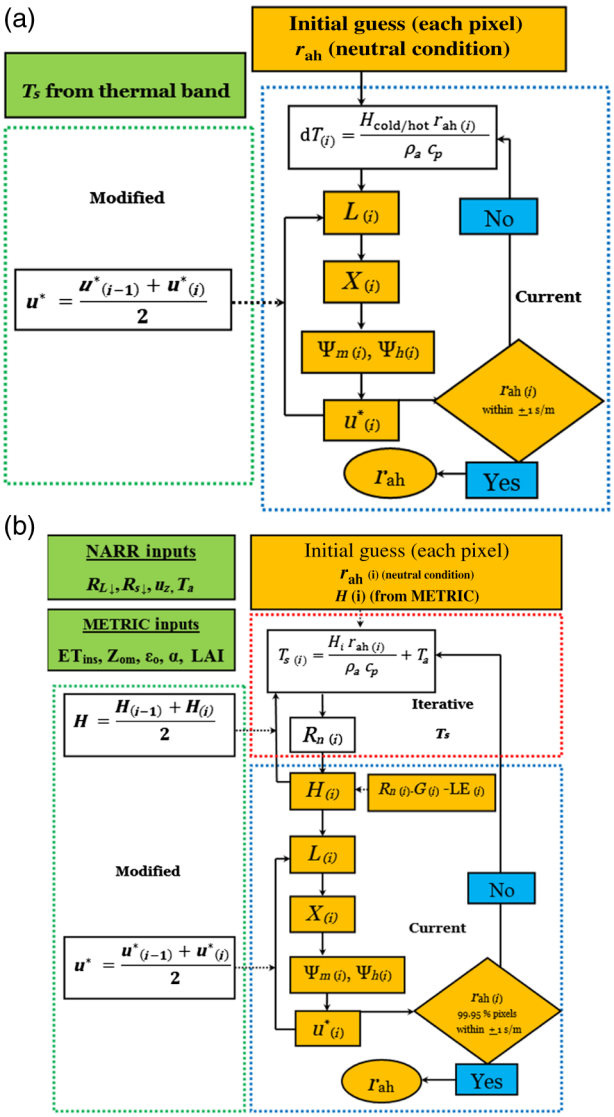

Fig. 2 (a) Surface energy balance and stability correction using current iterative technique and modified version of known H for hot and cold pixels (green dotted box—modified version and blue dotted box—current version). (b) Surface energy balance and stability correction using current iterative technique and modified version, where surface temperature is iteratively calculated (green dotted box—modified version, blue dotted box—current technique, and red dotted box—iterative surface temperature).

for all the pixels is computed based on the linear relationship dT and T_s. We also develop a similar procedure (METRIC and SEBAL) to calculate all of the H pixels with a stability correction. Using a neutral stability condition, the first iteration generates the set of data for the next iterations. As u^* is in a nested loop, we averaged u^* from the current time-step $[u^*_{(i)}]$ and the previous time-step $[u^*_{(i-1)}]$, which is stored for each iteration. In this case, latent heat flux (LE) is calculated as a residual after calculation of H for all pixels from the surface energy balance. The METRIC model, computational procedure of dT of hot and cold pixels, and H (case I) are described.[17,45]

3.2 *Case II—Iteratively Calculated Surface Temperature (T_s)*

In an instance when T_s is unavailable (calculation of surface energy balance fluxes other than satellite overpass time), it can be calculated iteratively inside the surface energy balance.[43,46] (1) We utilized the modification (backward averaging) to test if the convergence can be achieved in this instance [Fig. 2(b)]. (2) We also tested the modified version for the two-source surface energy balance, where soil evaporation and canopy transpiration are calculated iteratively inside the surface energy balance.[46] In this instance, the averaging of H along with u^*, which are in a nested loop in the surface energy balance, significantly reduced the iterations and avoided the nonconvergence. As the majority of the surface energy balance components are dominated by T_s, in the instance where T_s is not available, the convergence of surface energy balance might be complicated.

Even if cases I and II adopt different procedures to calculate the final fluxes, both utilize a similar procedure for stability correction. The objective here is to demonstrate that the modification of the current iterative version would ultimately help to accelerate the convergence process.

3.3 *Case II Methodology*

The MO stability length (L) can be calculated either from an iterative procedure using wind profiles, temperature, and humidity or through more complicated measurements of wind speed, sensible heat flux, and latent heat flux.[47] In both the above-mentioned cases (cases I and II), the MO length (L) is iteratively computed from Eq. (2) [Figs. 2(a) and 2(b)].

$$L = -\frac{c_{\mathrm{p}} T_{\mathrm{s}} \rho_{\mathrm{a}} u^{*3}}{kgH}, \tag{2}$$

where L is in meters, c_p is the specific heat capacity of air [J/(kg K)], T_s is the surface temperature (K), ρ_a is the density of moist air (kg/m^3), u^* is the friction velocity (m/s), k is the von Kármán constant with a value of 0.41, g is the acceleration due to gravity (m/s^2), and H is in W/m^2. Friction velocity (u^*) with a momentum correction is computed according to Eq. (3). Friction velocity (u^*) is needed to compute the aerodynamic resistance, as well as L; so this parameter is in a nested loop [Figs. 2(a) and 2(b)].

$$u^* = \frac{k u_z}{\ln\left(\frac{z-d}{Z_{\mathrm{om}}}\right) - \psi_{\mathrm{m}}\left(\frac{z-d}{L}\right)}, \tag{3}$$

where height (z) is the height of the wind speed (u_z) and T_a measurements, d is the zero plane displacement (m), Z_{om} is in meters, and ψ_m is the stability correction for momentum transport (unitless). The integrated stability corrections for momentum (ψ_m) and heat transport (ψ_h) are computed based on the equations in Refs. 48 and 49. Equation (4) is used to calculate r_{ah} under conditions requiring stability correction.[50] These variables should be revised until the components of the surface energy balance converge within prescribed limits between successive iterations. When r_{ah} of a current iteration is within ± 1 s/m to the previous iteration for 99.98% of all of the Landsat pixels, iteration was stopped. The convergence of r_{ah} indicates the convergence

of the surface energy balance components as it confirms the progression of stability correction [Eq. (1)].

$$r_{\mathrm{ah}} = \frac{\left[\ln\left(\frac{z-d}{Z_{\mathrm{om}}}\right) - \psi_m\left(\frac{z-d}{L}\right)\right]\left[\ln\left(\frac{z-d}{Z_{\mathrm{oh}}}\right) - \psi_h\left(\frac{z-d}{L}\right)\right]}{k^2 u_z}, \tag{4}$$

where Z_{oh} is the roughness length of heat transfer (m). In the situation where T_s is calculated inside the surface energy balance, it can be calculated by rearranging Eq. (1) [Eq. (5)]. Initial H can be utilized from the METRIC model as a preliminary guess. In this case, both H and T_s are unknown and need to be calculated inside the surface energy balance.

$$T_s = \frac{H r_{\mathrm{ah}}}{\rho_a c_p} + T_a, \tag{5}$$

where H can be recalculated and updated as a residual in each iteration using the below equation.

$$H = R_n - G - \mathrm{LE}, \tag{6}$$

where H, G, R_n, and LE are in $\mathrm{W/m^2}$. In Eq. (6), R_n is computed from the surface radiation balance equation [Eq. (7)] (for cases I and II).

$$R_n = R_{\mathrm{s}\downarrow} - \alpha R_{\mathrm{s}\downarrow} + R_{\mathrm{L}\downarrow} - R_{\mathrm{L}\uparrow} - (1-\varepsilon_{\mathrm{o}})R_{\mathrm{L}\downarrow}, \tag{7}$$

where $R_{s\downarrow}$, $R_{L\uparrow}$, and $R_{L\downarrow}$ are in $\mathrm{W/m^2}$. Albedo (α) and broadband emissivity (ε_{o}) are fractional numbers, which are unitless. Outgoing long-wave radiation ($R_{L\uparrow}$) in Eq. (7) is computed using the Stefan–Boltzmann equation [Eq. (8)] (for cases I and II).

$$R_{L\uparrow} = T_s^4 \sigma \varepsilon_{\mathrm{o}}, \tag{8}$$

where $R_{L\uparrow}$ is in $\mathrm{W/m^2}$, ε_{o} is the broadband emissivity, σ is the Stefan–Boltzmann constant (5.67×10^{-8} $\mathrm{W/m^2/K^4}$), and T_s is in Kelvin. G is computed based on H, R_n, and LAI,[17,51] which are in a nested loop as both R_n and H are iteratively calculated [Eq. (9)]. Max symbol in Eq. (9) selects the maximum values between H and R_n.

$$G = \begin{cases} 0.05 + 0.18\mathrm{e}^{-0.521\mathrm{LAI}}, & \text{if LAI} \geq 0.5 \\ \max(0.4H, 0.15R_n), & \text{otherwise} \end{cases}, \tag{9}$$

LE (λ ET) in Eq. (6) is the product of ET and latent heat of vaporization (λ). The latent heat of vaporization (λ) is computed from Ref. 52 [Eq. (10)]. We utilized $\mathrm{ET_{ins}}$ from METRIC to demonstrate the convergence procedure (case II); if not, it needs to be computed iteratively inside the surface energy balance.

$$\lambda = [2.501 - 0.00236(T_s - 273)] \times 10^6, \tag{10}$$

where λ is the latent heat of vaporization (J/kg) and T_s is in Kelvin. The convergence procedure follows Eqs. (2), (3), and (4).

4 Results and Discussion

The meteorological parameters u_z, T_a, $R_{S\downarrow}$, and $R_{L\downarrow}$ may vary little or are assumed to be the same for all land-use classes, if they lie in the same NARR pixel (or are taken from weather stations), but the convergence of individual pixels may vary with the characteristics of the surface (T_s, Z_{om}, Z_{oh}, and dT). We tested both the cases, i.e., utilizing thermal T_s and iteratively calculated T_s [Figs. 2(a) and 2(b), respectively] entirely to understand the convergence. Figure 3 shows the convergence of different Landsat pixels for various weather and surface conditions, where Figs. 3(a)–3(e) adopt the procedure in case I (convergence of hot and cold pixels), while the

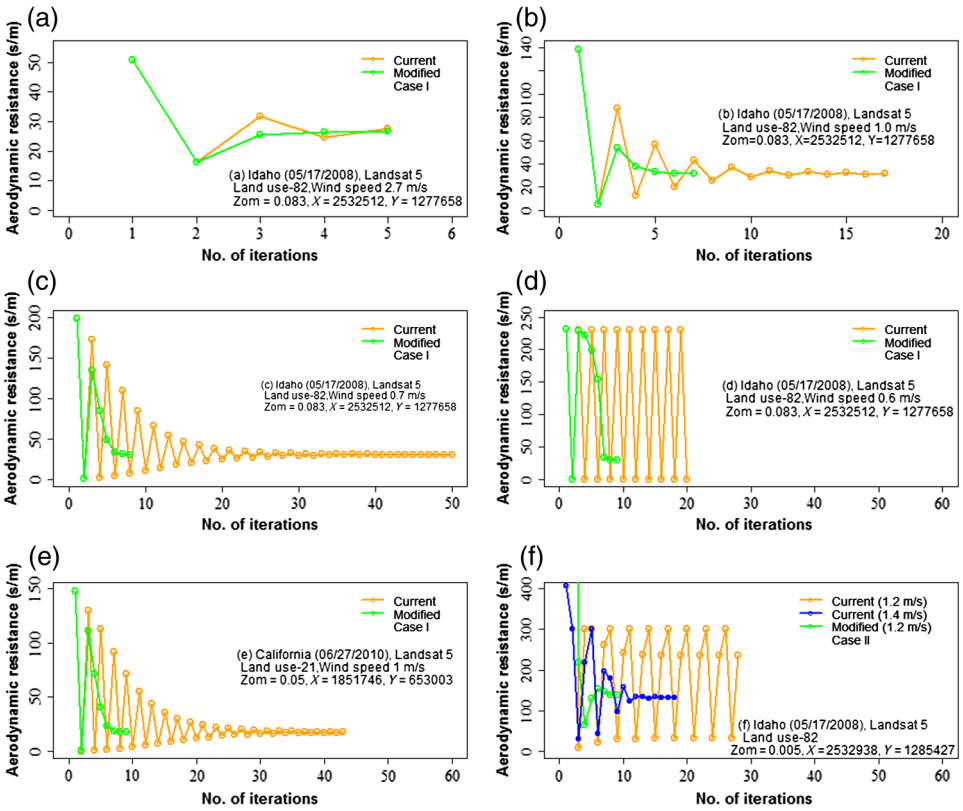

Fig. 3 Convergence pattern of aerodynamic resistance using current iterative technique and modified version for various surface and weather conditions. (a) Wind speed-2.7 m/s (case I-Idaho). (b) Wind speed-1 m/s (case I-Idaho). (c) Wind speed-0.7 m/s (case I-Idaho). (d) Wind speed-0.6 m/s (case I-Idaho). (e) Wind speed-1 m/s (case I-California). (f) Wind speed-1.4, 1.2 m/s (case II-Idaho).

rest of the results correspond to case II. These pixels were selected for different dates in Idaho and California. The estimated wind speed at 200 m blending height was ~2.7 m/s [Fig. 3(a)] for May 17, 2008, at Idaho. We lowered the wind speed to 1 m/s [Fig. 3(b)], 0.7 m/s [Fig. 3(c)], and 0.6 m/s [Fig. 3(d)] to understand the behavior of the same pixel. Table 1 shows the convergence of r_{ah} of the candidate cold and hot pixel [Figs. 3(a)–3(e)] from the METRIC as the spreadsheet only calculates up to 10 iterations. If the iteration is ceased within 10 iterations or wind speed is increased to get convergence, the values of dT, H, and ultimately LE will be influenced. We then allowed the continuation of the iterations until convergence with the identical procedure applied in spreadsheet was achieved [Fig. 2(a)]. This particular pixel was able to get convergence up to 0.7 m/s [Fig. 3(c)] from both versions. Below 0.7 m/s [Fig. 3(d)], the pixel was unable to get convergence from the current version. The convergence of this pixel needed up to 30 iterations [Fig. 3(c)] from the current version, while after modification, the pixel converged within a few iterations (three to eight iterations) in all instances. Figure 3(e) shows a candidate hot pixel on June 27, 2007, in the California study area, which shows a similar behavior at a low wind speed of 1 m/s. This nonconvergence would either overestimate or underestimate r_{ah}, which ultimately affects the values of dT, H, and finally LE. The larger error in r_{ah} would probably generate the artifacts in the surface energy flux components. The MO scaling (u^* and T^*, T^* is the dynamical temperature) is designed for shear-driven turbulence influenced by stratification, which is not adequate for such situations. The empirical similarity functions utilized have a limited range of validity ($z/L < -2$, z is the blending height) and should not be used beyond this range. Remedies should be sought by combining with other parameterizations.[53,54]

Aerodynamic resistance (r_{ah}) converged in an oscillating behavior with the current iterative technique, but after averaging, oscillation behavior was eliminated (Fig. 3). With the decreased

Table 1 Convergence of candidate cold and hot pixels from METRIC spreadsheet: case I.

Cold	Cold	Cold	Cold	Hot
r_{ah}, s/m	r_{ah}, s/m	r_{ah}, s/m	r_{ah}, s/m	r_{ah}, s/m
Fig. 3(a)	Fig. 3(b)	Fig. 3(c)	Fig. 3(d)	Fig. 3(e)
Wind speed				
2.7 m/s	1 m/s	0.7 m/s	0.6 m/s	1 m/s
50.76	138.43	197.76	230.71	138.98
16.63	5.11	1.53	0.26	4.216
31.76	86.65	168.82	229.74	89.58
24.76	12.83	3.12	0.24	10.51
27.78	56.31	137.43	229.98	58.35
26.45	20.33	5.51	0.23	17.20
27.03	43.01	106.58	230.05	43.562
26.78	25.51	8.63	0.23	22.32
26.89	37.17	82.11	230.06	36.73
26.84	28.53	12.19	0.23	31.76

mechanical mixing, i.e., u_z, the aerodynamic resistance (r_{ah}) increased [Figs. 3(a)–3(e) and Table 1). For higher wind speed, i.e., ~2.7 m/s at 200 m, the convergence behavior was similar before and after modifications [Fig. 3(a)]. Figure 3(f) shows the convergence pattern of the selected individual pixel from the procedure described in case II. In this instance, this particular pixel was able to get convergence up to a wind speed of 1.4 m/s (we decreased the wind speed from 1.81 m/s). This particular pixel is at a state of nonconvergence when the wind speed is ~1.2 m/s from the current version. As described earlier, when T_s is calculated inside the surface energy balance, conversion can be complicated compared to case I. We evaluated the convergence patterns of other surface energy flux components (T_s, G, R_n, H, u^*, L, ψ_h, and ψ_m) in case II. These surface energy components closely followed the pattern of r_{ah}, i.e., oscillating behavior with the current version. Apart from these pixels shown in Fig. 3, we also tested numerous other pixels on June 18, 2008, for Landsat 5 (Idaho) and August 22, 2010, for Landsat 7 (California) for cases I and II. The results are consistent with the findings shown in Fig. 3.

In the year 2008, out of ~732 h (satellite overpass hours), ~141 h have wind speeds below 2 m/s (at 2 m height, from Rupert AgriMet, Idaho, which is the nearest weather station to the Idaho study area). This indicates that the satellite-based ET estimations may be frequently affected by low wind speed conditions. In this section, discussion was carried out for the convergence behavior of all of the Landsat pixels of the study area on May 17, 2008, in Idaho. These pixels represent a number of different NLCD classes with various meteorological conditions. The wind speeds of the upper right pixel, lower right pixel, and lower left pixel were 1.45, 1.59, and 1.83 m/s apart from the upper left main study area with 1.81 m/s (Fig. 2) from Idaho. We set a hypothetical wind speed of ~1.3 m/s at 30 m blending height with the rest of data from NARR. We also tracked the real-time simulation of the convergence of all of the pixels for this specific case of Idaho as an illustration using case II (Fig. 4). These results should be taken with caution as the computation time may vary with the hardware processor, the size of the area of interest, and probably the scripting language and platform. Only 96% of the entire Landsat pixels were converged in 50 iterations in ~37 min with the current version (Fig. 4). Conversely, 99.98% of the all of the Landsat pixels were converged within eight iterations using the modified version in ~6 min using python-based arcScript algorithms with a regular i7, 2.4 GHz processor speed computer. We lowered the wind speed to test

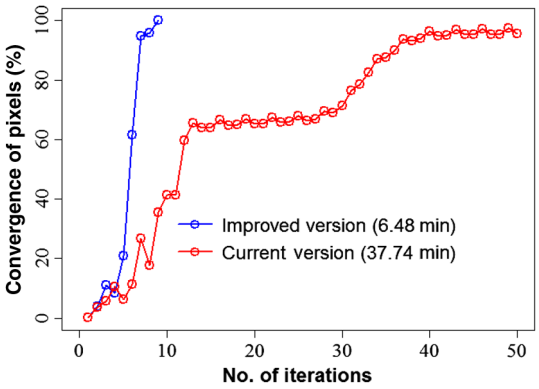

Fig. 4 Real-time simulation of convergence surface energy balance components represented by aerodynamic resistance using current and modified version—case II (Idaho, 2008).

the applicability of this modification and it shows a consistent result. Apart from backward averaging, proper boundary conditions in components of the surface energy balance were utilized to avoid extreme numbers as well as the artifacts (Table 2). We also tested this procedure for convergence of H in METRIC and SEBAL [after dT calculation, Fig. 2(a)] and the two-source source energy balance, which satisfactorily helped for the convergence process.

Table 2 Fluxes, parameters, variables, and boundary conditions of the model for case II.

Parameters	Symbol	Min	Max	Units
Incoming solar radiation	$R_{S\downarrow}$	—	—	W/m^2
Incoming long-wave radiation	$R_{L\downarrow}$	—	—	W/m^2
Net radiation	R_n	—	—	W/m^2
Height of vegetation	h	—	—	m
Measurement height (blending height)	z	—	—	m
MO parameter	X	—	—	—
Stability correction parameter of momentum	ψ_m	—	—	—
Stability correction parameter of heat	Ψ_h	—	—	—
Surface temperature	T_s	265	350	K
Air temperature at blending height	T_a	—	—	K
Wind speed at blending height	u_z	—	—	m/s
Instantaneous ET	ET_{ins}	0.0001	1.4 Ref_ET	mm/h
Sensible heat flux	H	−200	600	W/m^2
Ground heat flux	G	−150	200	W/m^2
Latent heat flux	LE	—	—	W/m^2
Friction velocity	u^*	1	500	m/s
Aerodynamic resistance	r_{ah}	0.01	500	s/m
Albedo	α	—	—	—
Zero plane displacement	d	—	—	m
Roughness length of momentum	Z_{om}	—	—	m
Roughness length of heat	Z_{oh}	—	—	m

5 Conclusions

Remote sensing based surface energy balance components often need to be iteratively solved. These results confirmed that averaging the components of the surface energy balance that are in the nested loop helped to accelerate the process and acquire the convergence even in a low wind speed condition. As different surface energy balance models utilize various kinds of data sets, this modification can probably help for convergence for other models, too. When wind speed is ~1.3 m/s, the current iterative technique was not able to get convergence of all of the Landsat pixels. In contrast, an improved version was able to get convergence of the surface energy flux parameters in minimal iterations. This technique helps to reduce the uncertainty in flux calculation (under- or overestimation of surface energy components) induced by the nonconvergence and can increase the accuracy of surface energy balance components, which is especially vital in arid and semiarid conditions. This improved version can be implemented by various operational ET models without major alterations of their present algorithms.

Acknowledgments

This study was supported by Dr. Richard G. Allen, University of Idaho. Appreciation is extended to Clarence Robison for the discussion of the code and water resources research group of Kimberly R&E, University of Idaho.

References

1. Y. A. Liou and S. K. Kar, "Evapotranspiration estimation with remote sensing and various surface energy balance algorithms—a review," *Energies* **7**(5), 2821–2849 (2014).
2. R. Lemeur and L. Zhang, "Evaluation of three evapotranspiration models in terms of their applicability for an arid region," *J. Hydrol.* **114**(3), 395–411 (1990).
3. H. DehghaniSanij, T. Yamamoto, and V. Rasiah, "Assessment of evapotranspiration estimation models for use in semi-arid environments," *Agric. Water Manage.* **64**(2), 91–106 (2004).
4. R. K. Goyal, "Sensitivity of evapotranspiration to global warming: a case study of arid zone of Rajasthan (India)," *Agric. Water Manage.* **69**(1), 1–11 (2004).
5. S. A. Kurc and E. E. Small, "Dynamics of evapotranspiration in semiarid grassland and shrubland ecosystems during the summer monsoon season, central New Mexico," *Water Resour. Res.* **40**(9), W09305 (2004).
6. B. Zhang et al., "Comparison of three evapotranspiration models to Bowen ratio-energy balance method for a vineyard in an arid desert region of northwest China," *Agric. For. Meteorol.* **148**(10), 1629–1640 (2008).
7. P. J. Mitchell et al., "Partitioning of evapotranspiration in a semi-arid eucalypt woodland in south-western Australia," *Agric. For. Meteorol.* **149**(1), 25–37 (2009).
8. R. Tang, Z. L. Li, and B. Tang, "An application of the T_s–VI triangle method with enhanced edges determination for evapotranspiration estimation from MODIS data in arid and semi-arid regions: implementation and validation," *Remote Sens. Environ.* **114**(3), 540–551 (2010).
9. D. Deus, R. Gloaguen, and P. Krause, "Water balance modelling in a semi-arid environment with limited in-situ data: remote sensing coupled with satellite gravimetry, Lake Manyara, East African Rift, Tanzania," *Hydrol. Earth Syst. Sci. Discuss.* **8**(5), 8737–8792 (2011).
10. X. Li et al., "Estimation of evapotranspiration in an arid region by remote sensing—a case study in the middle reaches of the Heihe River Basin," *Int. J. Appl. Earth Obs. Geoinf.* **17**, 85–93 (2012).
11. M. Cruz-Blanco, I. J. Lorite, and C. Santos, "An innovative remote sensing based reference evapotranspiration method to support irrigation water management under semi-arid conditions," *Agric. Water Manage.* **131**, 135–145 (2014).
12. J. Xia et al., "Satellite-based analysis of evapotranspiration and water balance in the grassland ecosystems of dryland East Asia," *PLoS One* **9**(5), e97295 (2014).

13. M. Alazard et al., "Estimating evaporation in semi-arid areas facing data scarcity: example of the El Haouareb dam (Merguellil catchment, Central Tunisia)," *J. Hydrol. Reg. Stud.* **3**, 265–284 (2015).
14. M. Shanafield et al., "Field comparison of methods for estimating groundwater discharge by evaporation and evapotranspiration in an arid-zone playa," *J. Hydrol.* **527**, 1073–1083 (2015).
15. E. P. Glenn et al., "Integrating remote sensing and ground methods to estimate evapotranspiration," *Crit. Rev. Plant Sci.* **26**(3), 139–168 (2007).
16. M. García et al., "Actual evapotranspiration in drylands derived from in-situ and satellite data: assessing biophysical constraints," *Remote Sens. Environ.* **131**, 103–118 (2013).
17. R. G. Allen, M. Tasumi, and R. Trezza, "Satellite-based energy balance for mapping evapotranspiration with internalized calibration (METRIC)—model," *J. Irrig. Drain. Eng.* **133**(4), 380–394 (2007).
18. W. G. M. Bastiaanssen et al., "A remote sensing surface energy balance algorithm for land (SEBAL). 1. Formulation," *J. Hydrol.* **212**, 198–212 (1998).
19. Z. Su, "The surface energy balance system (SEBS) for estimation of turbulent heat fluxes," *Hydrol. Earth Syst. Sci. Discuss.* **6**(1), 85–100 (2002).
20. S. P. Oncley et al., "The energy balance experiment EBEX-2000. Part I: overview and energy balance," *Boundary Layer Meteorol.* **123**(1), 1–28 (2007).
21. T. Foken, "The energy balance closure problem: an overview," *Ecol. Appl.* **18**(6), 1351–1367 (2008).
22. P. Pieri and M. Fuchs, "Comparison of Bowen ratio and aerodynamic estimates of evapotranspiration," *Agric. For. Meteorol.* **49**(3), 243–256 (1990).
23. A. E. Galinski and D. J. Thomson, "Comparison of three schemes for predicting surface sensible heat flux," *Boundary Layer Meteorol.* **72**(4), 345–370 (1995).
24. M. J. Best, "A model to predict surface temperatures," *Boundary Layer Meteorol.* **88**(2), 279–306 (1998).
25. F. Ács and M. Kovács, "The surface aerodynamic transfer parameterization method SAPA: description and performance analyses," *Idöjárás* **105**, 165–182 (2001).
26. F. Ács, "A comparative analysis of transpiration and bare soil evaporation," *Boundary Layer Meteorol.* **109**(2), 139–162 (2003).
27. F. S. Anslow et al., "Distributed energy balance modeling of South Cascade Glacier, Washington and assessment of model uncertainty," *J. Geophys. Res.* **113**(F2), 019 (2008).
28. E. H. Rambikur and J. L. Chávez, "Assessing inter-sensor variability and sensible heat flux derivation accuracy for a large aperture scintillometer," *Sensors* **14**(2), 2150–2170 (2014).
29. V. T. Chow, *Handbook of Applied Hydrology: A Compendium of Water Resources Technology*, McGraw-Hill, New York, R. L. Hanson, Evapotranspiration and droughts, R. W. Paulson et al., Compilers, National Water Summary, pp. 99–104 (1964).
30. R. L. Hanson, *Evapotranspiration and Droughts*, R. W. Paulson et al., Compilers, National Water Summary, pp. 99–104 (1988).
31. R. G. Allen, "Using the FAO-56 dual crop coefficient method over an irrigated region as part of an evapotranspiration inter comparison study," *J. Hydrol.* **229**(1), 27–41 (2000).
32. A. Ohmura and M. Wild, "Is the hydrological cycle accelerating?," *Science* **298**(5597), 1345–1346 (2002).
33. A. Porporato, E. Daly, and I. Rodriguez-Iturbe, "Soil water balance and ecosystem response to climate change," *Am. Nat.* **164**(5), 625–632 (2004).
34. M. Wild et al., "On the consistency of trends in radiation and temperature records and implications for the global hydrological cycle," *Geophys. Res. Lett.* **31**(11), L11201 (2004).
35. V. M. Alvarez et al., "Regional assessment of evaporation from agricultural irrigation reservoirs in a semiarid climate," *Agric. Water Manage.* **95**(9), 1056–1066 (2008).
36. J. C. B. Hoedjes et al., "Deriving daily evapotranspiration from remotely sensed instantaneous evaporative fraction over olive orchard in semi-arid Morocco," *J. Hydrol.* **354**(1), 53–64 (2008).
37. H. A. R. De Bruin, R. J. Ronda, and B. J. H. Van De Wiel, "Approximate solutions for the Obukhov length and the surface fluxes in terms of bulk Richardson numbers," *Boundary Layer Meteorol.* **95**(1), 145–157 (2000).

38. K. Abdella and D. Assefa, "Non-iterative surface flux parametrization for the unstable surface layer," *Atmos. Ocean* **43**(3), 249–257 (2005).
39. M. Pagowski, "An iterative solution of flux-profile relationships in the surface layer for regional model applications," *Atmos. Environ.* **40**(35), 6892–6897 (2006).
40. G. Koloskov, K. Mukhamejanov, and T. W. Tanton, "Monin–Obukhov length as a cornerstone of the SEBAL calculations of evapotranspiration," *J. Hydrol.* **335**(1), 170–179 (2007).
41. Y. Li et al., "An improved approach for parameterizing surface-layer turbulent transfer coefficients in numerical models," *Boundary Layer Meteorol.* **137**(1), 153–165 (2010).
42. J. Ban, Z. Gao, and D. H. Lenschow, "Climate simulations with a new air-sea turbulent flux parameterization in the National Center for Atmospheric Research Community Atmosphere Model (CAM3)," *J. Geophys. Res.* **115**(D1), D01106 (2010).
43. R. Dhungel et al., "Comparison of latent heat flux using aerodynamic methods and using the Penman–Monteith method with satellite-based surface energy balance," *Remote Sens.* **6**(9), 8844–8877 (2014).
44. F. Mesinger et al., "North American regional reanalysis," *Bull. Am. Meteorol. Soc.* **87**(3), 343–360 (2006).
45. R. G. Allen et al., *Satellite-Based Energy Balance for Mapping Evapotranspiration with Internalized Calibration (METRIC)—Application Manual*, University of Idaho, Kimberly, Idaho (2010).
46. R. Dhungel, "Time integration of evapotranspiration using a two source surface energy balance model using NARR reanalysis weather and satellite based METRIC data," PhD Thesis, University of Idaho, Kimberly, Idaho (2014).
47. B. Wilfried, *Evaporation into the Atmosphere: Theory, History and Applications*, Reidel, Dordrecht, The Netherlands (1982).
48. C. A. Paulson, "The mathematical representation of wind speed and temperature profiles in the unstable atmospheric surface layer," *J. Appl. Meteorol.* **9**, 857–861 (1970).
49. E. K. Webb, "Profile relationships: the log-linear range and extension to strong stability," *Q. J. R. Meteorolog. Soc.* **96**, 67–90 (1970).
50. A. S. Thom, "Momentum, mass and heat exchange of vegetation," *Q. J. R. Meteorolog. Soc.* **98**, 124–134 (1972).
51. R. Allen et al., "Satellite based ET estimation in agriculture using SEBAL and METRIC," *Hydrol. Process.* **25**, 4011–4027 (2011).
52. L. P. Harrison *Humidity and Moisture: Fundamental's Concepts and Definitions Relating to Humidity*, A. Wexler, Ed., Reinhold Publishing Co., New York (1963).
53. A. A. Grachev, C. W. Fairall, and S. S. Zilitinkevich, "Surface-layer scaling for the convection-induced stress regime," *Boundary Layer Meteorol.* **83**(3), 423–439 (1997).
54. U. Schumann, "Minimum friction velocity and heat transfer in the rough surface layer of a convective boundary layer," *Boundary Layer Meteorol.* **44**(4), 311–326 (1988).

Ramesh Dhungel is a postdoctoral scholar/water resources engineer at the University of California, Merced. He received his MS and PhD degrees in civil engineering at the University of Idaho. His research focus on various water resources management topics like surface and ground water, biomicrometerology, and atmospheric and environmental modeling using remote sensing, and geospatial tools.

Richard G. Allen is a professor of water resources engineering at the University of Idaho in the Department of Biological and Agricultural Engineering. He received his PhD at the University of Idaho. He has published numerous articles and books about evapotranspiration, remote sensing of evapotranspiration, and surface energy balance. He is a current member of the NASA Landsat Team.

Ricardo Trezza is an associate professor in the University of Idaho Department of Biological and Agricultural Engineering. He received his PhD at Utah State University. His research focuses on the evapotranspiration, remote sensing of evapotranspiration, and irrigation engineering.